14. C. S. Breed, J. F. McCauley, M. J. Grolier, *Geophys. Res.*, in press.
15. J. F. McCauley, C. S. Breed, M. J. Grolier, *NASA Tech. Memo. 82385* (1980), pp. 312–313.
16. P. S. Chavez, Jr., G. L. Berlin, W. B. Mitchell, in *Proceedings, Sixth Symposium on Remote Sensing of Earth Resources* (Tullahoma, Tennessee, March 1977), pp. 259–275.
17. J. F. McCauley, C. S. Breed, M. J. Grolier, *NASA Contract. Rep. CR3611*, in press.
18. B. Issawi, abstract of papers presented at the Geological Society of America Annual Meeting, New Orleans, 19 October 1982.
19. H.-J. Pachur, in *The Geology of Libya, Second Symposium on the Geology of Libya, Tripoli, 16 to 21 September 1978*, M. J. Salem and M. T. Busrewil, Eds. (Academic Press, New York, 1980), vol. 3, pp. 781–788.
20. R. Said, *The Geological Evolution of the River Nile* (Springer-Verlag, New York, 1981).
21. K. W. Butzer and C. L. Hansen, *Desert and River in Nubia: Geomorphology and Prehistoric Environments at the Aswan Reservoir* (Univ. of Wisconsin Press, Madison, 1968).
22. L. Berry and A. J. Whiteman, *Geogr. J.* **134**, (part 1), 1 (1968).
23. F. W. Van Eysinga, *Geological Timetable* (Elsevier, New York, 1975).
24. R. F. Giegengack, thesis, Yale University (1968).
25. F. Hassan, *Quat. Res. (N.Y.)* **6**, 425 (1976).
26. A. T. Grove and A. Warren, *Geogr. J.* **134** (part 2), 194 (1968).
27. M. Servant and S. Servant-Vildary, in (*3*), pp. 133–162.
28. D. Adamson and F. Williams, in (*3*), pp. 225–252.
29. W. B. K. Shaw, *Geogr. J.* **87**, 193 (1936).
30. M. A. J. Williams, D. A. Adamson, F. M. Williams, W. H. Morton, D. E. Parry, in (*3*), pp. 305–337.
31. G. A. Boulenger, *Nature (London)* **72**, 413 (1905).
32. O. H. Stigand, *Geogr. J.* **48**, 145 (1916).
33. A. Holmes, *ibid.*, p. 149.
34. J. Maley, *C. R. Acad. Sci. Ser. D* **276**, 1673 (1973).
35. E. Raisz, Land Form Map of North Africa, 48 by 22 inches (Boston, Mass., 1952).
36. J. F. McCauley, in *Mantles of the Earth and Terrestrial Planets*, S. K. Runcorn, Ed. (Interscience, New York, 1967), pp. 431–460.
37. D. E. Wilhelms and J. F. McCauley, Geological Map of the Near Side of the Moon: U.S. Geological Survey, Geologic Atlas of the Moon, Near Side of the Moon, Map I-703 (scale 1:5,000,000).
38. B. Issawi, *Gen. Egypt. Org. Geol. Res. Min. Geol. Surv. Pap.* **46** (1969).
39. J. Ball, *Geogr. J.* **70**, 105 (1927).
40. W. J. E. van de Graaff, R. W. A. Crowe, J. A. Bunting, M. J. Jackson, *Z. Geomorphol.* **21** (No. 4), 379 (1977).
41. F. Wendorf, R. Schild, R. Said, C. V. Haynes, A. Gautier, M. Kobusiewicz, *Science* **193**, 103 (1976).
42. F. Wendorf and Members of the Combined Prehistoric Expedition, *Geogr. J.* **143** (part 2), 211 (1977).
43. C. V. Haynes, P. J. Mehringer, Jr., S. A. Zaghloul, *Geogr. J.* **145**, 437 (1979).
44. W. P. McHugh, "Late Prehistoric cultural adaptation in Southwest Egypt and the problem of the Nilotic origins of Saharan cattle pastoralism," *J. Am. Res. Ctr. Egypt* **11**, 9 (1974).
45. W. P. McHugh, *Geogr. J.* **146**, 64 (1980).
46. ——, *NASA Contract. Rep. CR 3611*, in press.
47. G. Caton-Thompson and E. W. Gardner, *Geogr. J.* **80**, 369 (1932).
48. J. D. Clark in (*3*), pp. 527–582.
49. A. B. Smith, in (*3*), pp. 489–501.
50. E. M. Eliason, P. S. Chavez, Jr., L. A. Soderblom, *Geology* **5** (No. 2), 231 (1974).
51. C. S. Breed, N. S. Embabi, H. A. El-Etr, M. J. Grolier, *Geogr. J.* **146**, 88 (1980); C. S. Breed and T. Grow, *U.S. Geol. Surv. Prof. Pap. 1052* (1979), pp. 253–302.
52. A. Warren, *Z. Geomorphol. Suppl.* **10**, 154 (1970).
53. J. R. Parsons, *Am. Antiq.* **33**, 80 (1968); —— and N. P. Psuty, *ibid.* **40**, 259 (1975).
54. D. Henning and H. Flohn, *Climate Aridity Index Map: United Nations Conference on Desertification* (U.N. Environment Programme, Nairobi, Kenya, 1977).
55. C. Elachi, *Science* **209**, 1073 (1980).
56. B. Issawi, *Ann. Geol. Surv. Egypt* **1**, 53 (1971); ——, *ibid.* **3**, 25 (1973).
57. C. Elachi *et al.*, *Science*, **218**, 996 (1982).
58. J. E. Estes and D. S. Simonett, in *Manual of Remote Sensing*, R. C. Reeves, Ed. (American Society of Photogrammetry, Falls Church, Va. 1975), vol. 2, pp. 869–1076.
59. L. E. Roth and C. Elachi, *IEEE Trans. Antennas Propag.* **23**, 674 (1975).
60. C. Elachi, L. E. Roth, G. G. Schaber, *ibid.*, in press.
61. G. G. Schaber, G. L. Berlin, W. E. Brown, Jr., *Geol. Soc. Am. Bull.* **87**, 29 (1976).
62. P. Beckmann and A. Spizzichino, *The Scattering of Electromagnetic Waves from Rough Surfaces* (Macmillan, New York, 1963).
63. F. F. Sabins, *Remote Sensing, Principles and Interpretation* (Freeman, San Francisco, 1978).
64. R. Blom and C. Elachi, *J. Geophys. Res.* **86**, 3061 (1981).
65. W. H. Peake and T. L. Oliver, "The response of terrestrial surfaces at microwave frequencies:" *U.S. Air Force Avionics Lab. Rep. AFAL-TR-70-301* (1971).
66. R. K. Moore, in *Manual of Remote Sensing*, R. G. Reeves, Ed. (American Society of Photogrammetry, Falls Church, Va., 1975), vol. 1, pp. 399–538.
67. V. I. Myers, in *Manual of Remote Sensing*, R. G. Reeves, Ed. (American Society of Photogrammetry, Falls Church, Va., 1975), vol. 2, pp. 1715–1813.
68. A. R. Von Hippel, *Dielectrics and Waves* (Wiley, New York, 1954).
69. J. Chilar and F. T. Ulaby, *CRES Tech. Rep. 177-47 Univ. Kans. Cent. Res. (Lawrence, Kans.)* (1974).
70. G. Olhoeft, personal communication.
71. K. S. Sandford, *Geogr. J.* **82**, 210 (1933).
72. H. Cary, Transl., *The Histories of Herodotus*, book 2, *Euterpe* (Appleton, New York, 1899), pp. 86–87.
73. J. R. Lundien, *U.S. Army Eng. Waterways Exp. Stn. (Vicksburg, Miss.) Tech. Rep. 3-693* (1971).
74. L. F. Dellwig, *Mod. Geol.* **1** (No. 1), 65 (1969).
75. D. W. Strangway and G. R. Olhoeft, *Philos. Trans. R. Soc. London* **285**, 441 (1977).
76. J. Dubief, in *Die Sahara und ihre Randgebiete*, vol. 1, *Physiogeographie*, H. Schiffers, Ed. (Weltforom, Munich, 1971), pp. 227–348.
77. E. W. Gardner, *Q. J. Geol. Soc. London* **91**, (part 4), 479 (1935).
78. G. W. Murray, *Geogr. J.* **117**, 422 (1951).
79. Work described in this report was carried out under the auspices of the National Aeronautics and Space Administration Office of Non-Renewable Resources and the Planetary Program. Field support was provided by the Smithsonian Institution Foreign Currency Program in cooperation with the Egyptian Geological Survey and Mining Authority and Ain Shams University, Cairo. Support was also provided by the U.S. Geological Survey Office of International Geology and by the Geologic Framework Program. G. Olhoeft measured the electrical properties of our field samples. We thank F. Wendorf and members of the Combined Prehistoric Expedition for their hospitality in the field and W. P. McHugh, E. M. Shoemaker, B. Lucchitta, and D. Scott for their review of the manuscript and their helpful suggestions. W. P. McHugh accompanied us into the Arbain Desert in September 1982 to document relations of the radar subsurface topography to archeological remains.

20 August 1982; 10 October 1982

Mineral Identification from Orbit: Initial Results from the Shuttle Multispectral Infrared Radiometer

Abstract. *A shuttle-borne radiometer containing ten channels in the reflective infrared has demonstrated that direct identification of carbonates and hydroxyl-bearing minerals is possible by remote measurement from Earth orbit.*

The shuttle multispectral infrared radiometer (SMIRR) (*1*) (Fig. 1) was designed to obtain surface reflectance data in ten spectral bands (Fig. 2) in order to evaluate the usefulness of a future imaging system for remote mineral identification. In particular, the region 2.0 to 2.4 μm, which has a wealth of spectral absorption features, appeared to have potential for the identification of CO_3- and OH-bearing minerals such as clays (*2*).

SMIRR was carried aboard the second flight of the shuttle, on 12 to 14 November 1981. Of 186 minutes of data acquired, approximately 70 minutes, equivalent to 400,000 ten-channel spectra, were obtained under totally cloud-free conditions. Another 50 minutes of data were acquired in apparently cloud-free conditions, but the presence of high thin clouds cannot be ruled out (Fig. 3).

Two types of calibration procedures were applied to SMIRR. Absolute calibration of the instrument was carried out in the laboratory by use of a calibrated light source referenced to a National Bureau of Standards standard. Calibration during flight was performed by use of internal lamps. Before SMIRR was installed on the payload pallet, aircraft (*3*) and ground tests were conducted to determine its response to known targets. Figure 4 shows the results of laboratory tests with two clay minerals known to absorb between 2 and 2.5 μm. Continuous laboratory spectra were obtained with a Beckman 5240 spectrophotometer (*4*) modified for digital recording. In order to obtain spectral reflectance within the SMIRR filter bandpasses, the continuous spectra were weighted with filter transmission spectra produced on the same instrument according to

$$\frac{\sum_{n=1}^{k} F(\lambda_n)\, C(\lambda_n)}{\sum_{n=1}^{k} F(\lambda_n)}$$

where $F(\lambda_n)$ is the filter transmission, $C(\lambda_n)$ is the continuous spectrum of the sample measured in n intervals, and k is the number of intervals needed to cover the complete filter bandpass. Calibration tests were performed outdoors with pure mineral samples to determine the correspondence between SMIRR and laboratory measurements. Figure 5 shows the ten-channel spectra developed from continuous laboratory data and measurements made with the sun as a source. The difference in absolute reflectance between the laboratory and SMIRR mea-

0036-8075/82/1203-1020$01.00/0 Copyright © 1982 AAAS

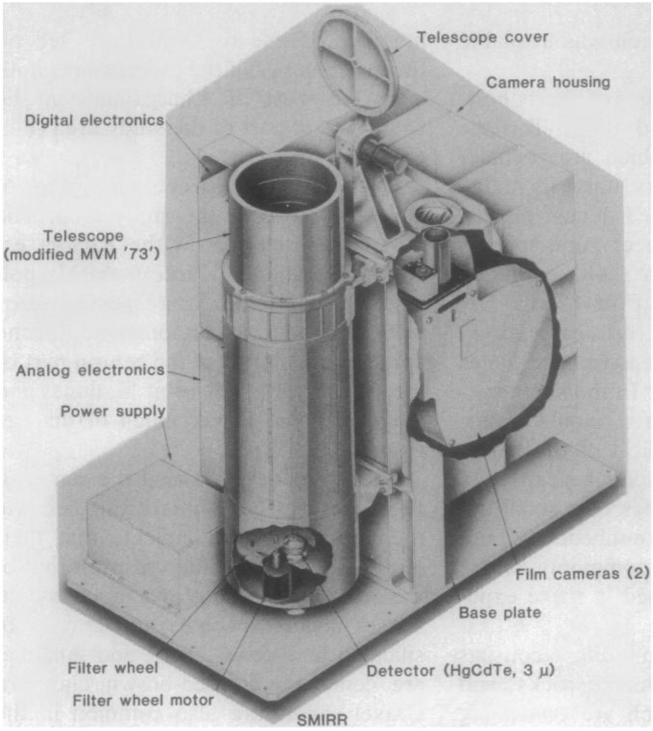

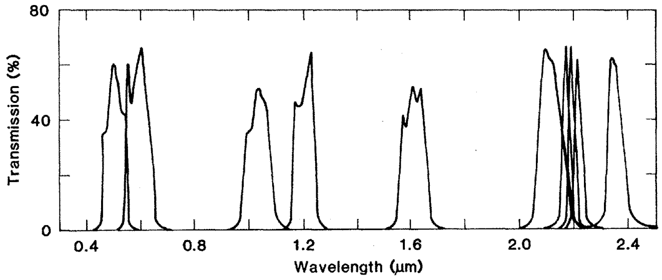

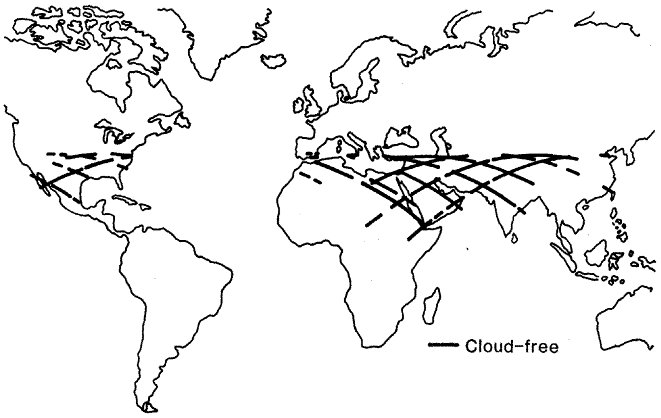

Fig. 1 (left). SMIRR instrument. Fig. 2 (upper right). Bandpasses for the ten SMIRR spectral filters. Fig. 3 (lower right). Map showing SMIRR flight coverage on 12 to 14 November 1981.

surements probably can be attributed to the fact that the laboratory measurements are made with an integrating sphere and the SMIRR measurement is bidirectional. However, the absolute values of reflectance are not as important in this analysis as the shape of the SMIRR spectra.

In order to provide an overview of the data and facilitate analysis, the continuous radiometer data were broken into line segments of 1.28 seconds each. Each 1.28-second segment is referred to as a line (L), and each point on the line represents a spectrum (S) of a 100-m-diameter spot on the ground. Each line contains 128 spectra, and the beginning of each line coincides with the center of the 16-mm frame of the camera containing black-and-white film. In this report the analysis is based on plots of radiometric profiles for individual channels or ratios of channels as a function of time and plots of individual ten-channel spectra.

The production of surface reflectance spectra from SMIRR requires knowledge of the intervening scattering and absorbing atmosphere. The LOWTRAN-5 atmospheric model (*5*) can be used to describe atmospheric absorption from the source to SMIRR, but this approach was not used because the model includes parameters such as visibility and water content at various altitudes, and these data are not available in the areas studied. Therefore, the technique used for normalization was to acquire surface samples and calibrate the SMIRR signal on the basis of laboratory spectra of the samples. This method is imperfect because the natural surface cannot be preserved during sampling and positions determined from prelaunch orbital predictions are imprecise. However, an attempt was made with samples taken near orbit 16 in the vicinity of Kharga, Egypt, and the results obtained are consistent with the mapped surface units. In future, in situ spectral reflectance measurements with a radiometer equipped with the SMIRR filter set should provide the most accurate calibration attainable.

For the initial analysis of SMIRR data a segment of orbit 16 covering the area between Kharga and Aswan, Egypt, was interpreted. This area was selected because the vegetation cover is negligible and the validity of the mineralogical de-

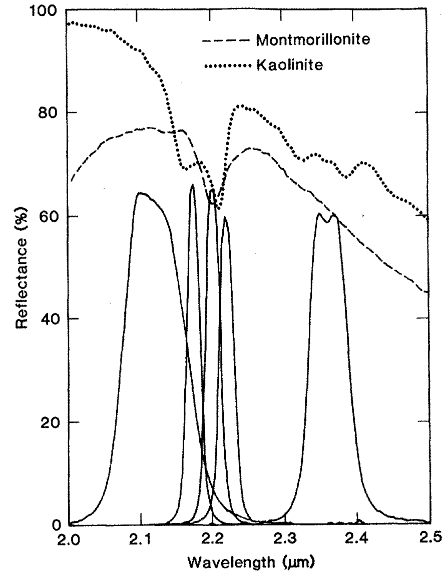

Fig. 4. High-resolution continuous laboratory spectra of two clays used in the SMIRR calibration shown in Fig. 5. Also shown are the measured bandpasses of five of the SMIRR filters.

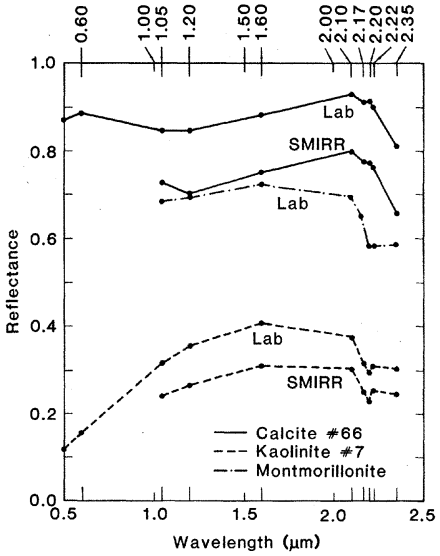

Fig. 5. Laboratory and SMIRR ground tests of standard samples. Two of the samples are the same as those in Fig. 4. Wavelength values at the top locate approximate centers of SMIRR spectral bands in micrometers.

terminations could be tested by reference to a recently published geologic map and to laboratory spectral reflectance measurements on samples collected in this area. The steps taken in the analysis were (i) normalization, using a spectrum from a bright area, which appeared on the photographs to be a dune and (ii) identification of the materials present in other areas along this orbit by comparing the appropriate SMIRR spectra with a collection of laboratory SMIRR spectra representing 60 mineral and rock types. Subsequently, the identifications were verified through discussions with F. El Baz (National Air and Space Museum, Smithsonian Institution, Washington, D.C.) and R. Said (Southern Methodist University, Dallas, Texas), both of whom are involved in geologic research and mapping in the area. Limited knowledge of the lithology of this part of Egypt was also used in the interpretation, but initially no specific mineralogical information was available for any line segment.

The study area consists of nearly horizontal Cretaceous and lower Tertiary sedimentary rocks, which are partially overlain by Quaternary units including extensive north-oriented dunes, playas, and gravel mounds, sheets, and spreads (Fig. 6). Nubia strata (color-coded in Fig. 6) underlie most of the Kharga Depression, but exposures are sparse owing to the presence of extensive sand dunes and playa deposits (*6*). In the southeastern part of the study area, tabular cross-bedded sandstone typical of the Nubia Formation (*7*) is exposed where orbit 16 crosses the lower slopes of a small upland area. Kaolinitic nonbedded sandstone with root traces commonly constitutes the uppermost bed in these exposures.

The unit coded green in Fig. 6 consists mainly of shale, carbonate rocks, and phosphatic beds, which are commonly limonitic. These rocks are exposed on the lower slopes of the escarpments both east and west of Kharga and in the southeastern part of the study area (Fig. 6).

Paleocene and Eocene units (Fig. 6) are widespread in the study area. The best exposures are on the Kharga escarpment, where a siliceous, highly polished, hackly weathering limestone caps the escarpment (*6*). Although the Eocene unit underlies most of the central part of the area traversed by orbit 16, dunes and gravel deposits cover much of this region.

The gravel deposits near the center of Fig. 6 are especially interesting because the SMIRR spectra indicate that their mineral content is different from that of the other units. The gravel mounds consist of angular pebbles and gravels of silicified limestone, chert, and flint that are cemented by red-brown clay (*6*). Gravel sheets are also common in the

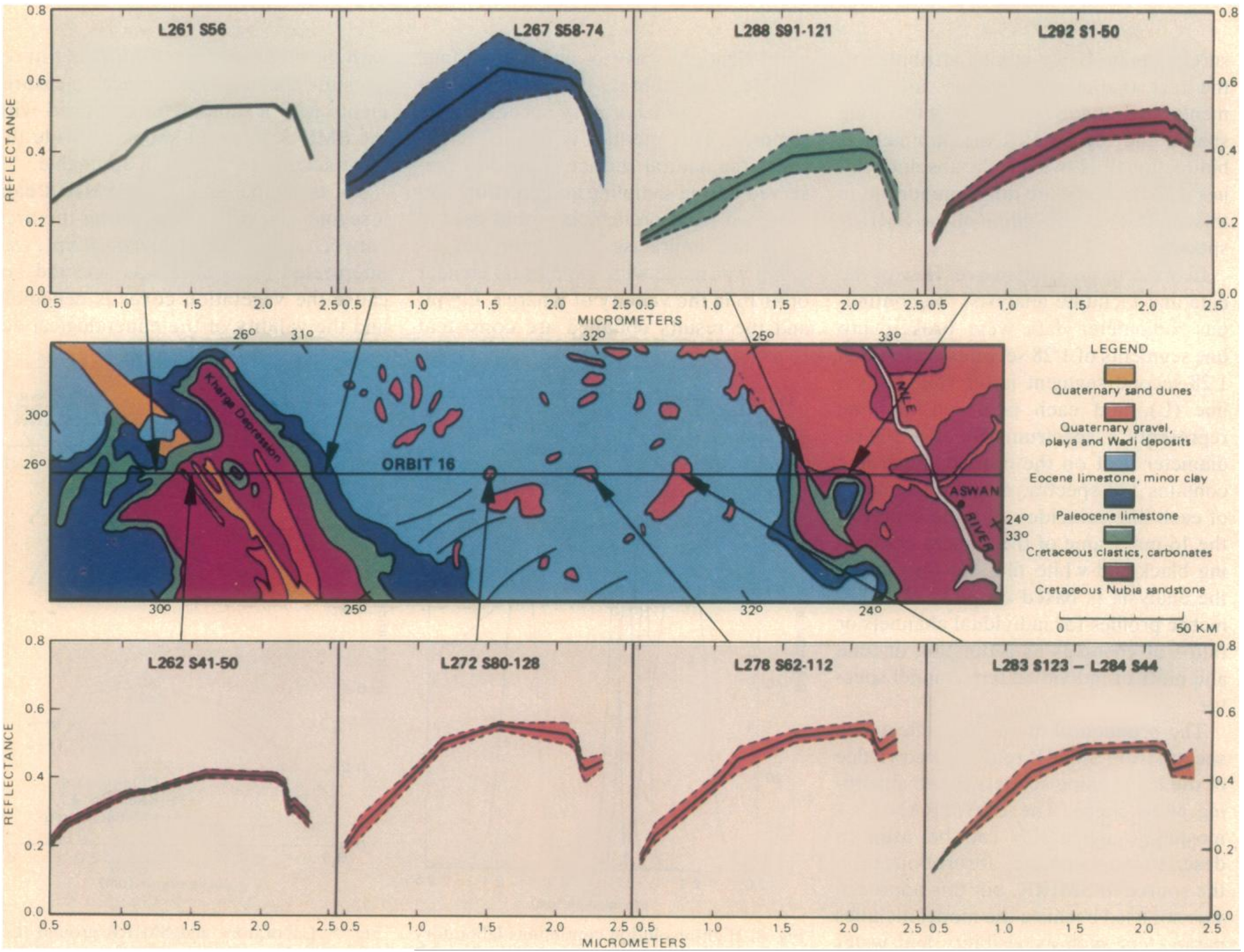

Fig. 6. Geological map of the Kharga-Aswan region of Egypt (*9*). Heavy solid lines show fault locations; lines are dashed where fault locations are approximate. Spectra are averages over segments of the orbit; the surrounding band of values indicates the standard deviation, except for L261–S56, which is a single spectrum.

central part of the study area, but either are not indurated or are cemented with tufa (*6*).

The SMIRR radiances along this segment of orbit 16 were normalized by using a spectrum for dune sand collected in the Kharga Depression (KS11, Fig. 7). This area is brighter than adjacent interdune areas, and x-ray diffraction analysis of the sample collected in this area indicates that it contains a substantial amount of calcite with minor kaolinite and gypsum, all of which have absorption features in the region 2.0 to 2.5 μm. Quartz, the major mineral component, is medium-grained and stained by iron oxide minerals. For normalization it was assumed (i) that deep shadows represent the zero-signal baseline and applying this baseline to the data cancels (to first order) any atmospheric scattering contribution and (ii) that sample area KS11 did not contain shadows. For orbit 16 the SMIRR signal values for each band were multiplied by the ratio of the laboratory-determined KS11 reflectance to the SMIRR signal value for the KS11 site. Because the attitude of the surface at KS11 is not known, there remains an additional, unknown multiplicative constant common to all bands.

The average SMIRR spectrum of S41–50 in line segment L262 (Fig. 6) represents a slightly darker interdune area in the Kharga Depression. These spectra have a more pronounced absorption in the 2.20-μm band than was measured by SMIRR in the adjacent KS11 site and therefore were interpreted as representing materials containing kaolinite. Subsequently, this interpretation was confirmed by F. El Baz and through x-ray analysis of a sample he collected at the KS9 site. The SMIRR laboratory spectra for the KS9 sample (Fig. 7) and the SMIRR spectra along line segment L262 (Fig. 6) are very similar to the SMIRR laboratory spectrum for kaolinite (Fig. 5).

In the further analysis of the SMIRR data, continuous plots of band ratios were examined for variations above or below the background values. Normalized spectra were calculated for parts of line segments where these variations were present. Then the source of the features observed in these spectra was determined by comparing the normalized SMIRR spectra with a library of simulated SMIRR spectra obtained in the laboratory. Care was taken to avoid shadows, which cause low signals that give spurious results.

An important consideration in the analysis was the general lithology of the study area. Although specific mineralogic information was not available for any particular 100-m-diameter area, the range of minerals that could cause the SMIRR spectral features was limited because only sedimentary rocks were present. For example, a 2.35-μm absorption band could be attributed to carbonate rocks, rather than to serpentine or some other mineral commonly associated with igneous or metamorphic rocks.

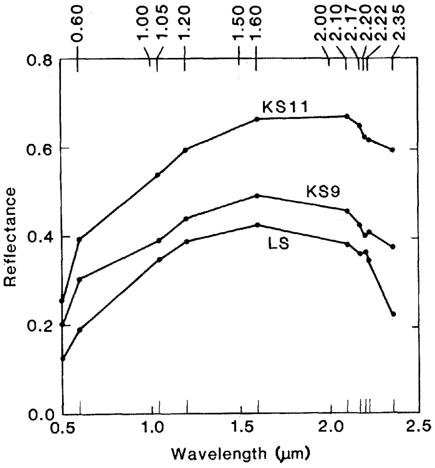

Fig. 7. Laboratory spectra of samples: KS11, dune sand; KS9, playa deposit; and LS, limestone from the Kharga region. Wavelength values at the top locate approximate centers of SMIRR spectral bands in micrometers.

Examination of continuous plots of the 2.20 μm/2.35 μm and 2.22 μm/2.35 μm ratios in the west-central part of the study area indicated the presence of carbonate rocks where these ratios increase abruptly. The increases are caused by low reflectance in the 2.35-μm SMIRR channel in the region covered by L267 S58–74, which is similar to the SMIRR spectrum obtained in the laboratory for calcite (Fig. 5). These SMIRR spectra correspond to the Paleocene and Eocene sequence exposed on the escarpment east of the Kharga Depression (Fig. 6). The highest values of these ratios in the southeastern part of the area are represented by the mean SMIRR spectrum calculated for spectra S91–121 in line segment L288 (Fig. 6). Again, the 2.35-μm reflectance is very low, strongly indicating the presence of carbonate rocks. The large standard deviation in this and in the L267 S58–74 mean SMIRR spectrum is probably due to brightness variations induced by topographic slope as well as shadows. The L288 S91–121 mean spectrum and the L261 S56 spectrum discussed by Goetz *et al.* (*8*) appear to represent carbonate rocks in the unit coded green in Fig. 6.

The mean SMIRR spectrum calculated for L292 S1–50 has a slightly depressed 2.20-μm reflectance (Fig. 6). Because of the similarity between the shape of this spectrum and the SMIRR laboratory spectrum for kaolinite (Fig. 5) and the presence of kaolinite in the Nubia strata in this region, we attribute this spectrum to the presence of kaolinite. The 2.20-μm feature is consistently present in spectra obtained for the area of Nubia strata (Fig. 6) situated between the eastern boundary of the Quaternary deposits and the Nile River.

The Quaternary deposits shown within the broad area near the center of Fig. 6 appear dark in the SMIRR 16-mm photographs and exhibit low reflectance in the continuous plots of the 1.60- and 2.20-μm channels. In this respect, these two areas are similar to the gravel mound represented by the mean SMIRR spectrum for L272 S80–128 (Fig. 6). Therefore, mean SMIRR spectra were calculated for these two areas. In both mean spectra (L278 S62–112 and L283 S123 to L284 S44), as in the L272 S80–128 spectrum, the reflectance in the 2.22-μm channel is lower than in the adjacent channels, and there is a large decrease in reflectance in the 2.20-μm channel relative to the 2.17-μm channel. The latter feature is similar to the SMIRR laboratory spectrum for montmorillonite (Fig. 5), but the 2.22-μm minimum is not as well defined in the laboratory spectrum. These spectral features are tentatively attributed, at least in part, to the presence of montmorillonite, but other minerals with absorption features in this part of the spectrum may explain the differences between the laboratory SMIRR spectrum for montmorillonite and the SMIRR spectra for these areas. The large 2.17 μm/2.20 μm ratio is attributed to the presence of montmorillonite because it is similar to the SMIRR laboratory spectrum for montmorillonite (Fig. 5). The red-brown clay matrix described in the gravel deposits, which underlies this area, may be montmorillonite, which commonly is coated with ferruginous oxides. This and the other mineralogical assignment proposed above must be verified by detailed field and laboratory studies.

SMIRR has acquired the first narrow-band spectral reflectance data from orbit in the short-wavelength infrared region. For the first time, materials other than limonite have been identified from orbit on the basis of intrinsic spectral features, as opposed to being simply separable on the basis of albedo differences in the visible and near-infrared. Direct identifications of carbonate, kaolinite-containing material, and possibly montmorillonite have been made. These results indicate that there is an excellent potential for future narrowband, spectral imaging systems for mineralogical mapping from orbital platforms.

ALEXANDER F. H. GOETZ
Jet Propulsion Laboratory,
Pasadena, California 91109
LAWRENCE C. ROWAN
MARGUERITE J. KINGSTON
U.S. Geological Survey,
Reston, Virginia 22092

References and Notes

1. The SMIRR instrument (Fig. 1) consists of a coaligned radiometer and two 16-mm cameras for positioning information. The radiometer consists of a reflecting telescope, spinning filter wheel, two thermoelectrically cooled HgCdTe detectors, and associated timing and signal conditioning electronics. Data were recorded on the shuttle payload tape recorder. The data were received from a 100-m-wide swath under the spacecraft. Field-of-view location within the camera frames is ±100 m. Data from the radiometer are oversampled so that sequentially obtained filter measurements can be resampled to provide spatially coincident data for all ten channels (A. F. H. Goetz, M. L. Brownell, J. C. Mahoney, D. B. Vane, in preparation).
2. A. F. H. Goetz and L. C. Rowan, *Science* **211**, 781 (1981); G. R. Hunt, *Geophysics* **42**, 501 (1977).
3. A. F. H. Goetz, *Proc. SPIE* **268**, 17 (1981).
4. Any use of trade names in this report is for descriptive purposes only and does not constitute endorsement by the National Aeronautics and Space Administration or the U.S. Geological Survey.
5. F. X. Kneizys *et al.*, *Air Force Geophys. Lab. Rep. AFGRL-TR-80-0067* (1980).
6. R. Said, *The Geology of Egypt* (American Elsevier, New York, 1962), part 3, pp. 67–76; W. C. Ward and K. C. McDonald, *Am. Assoc. Pet. Geol. Bull.* **63**, 975 (1979).
7. E. Klitzsch, J. C. Harms, A. Lesal-Nichol, F. List, *Am. Assoc. Pet. Geol. Bull.* **63**, 967 (1979).
8. A. F. H. Goetz, L. C. Rowan, M. J. Kingston, in *1982 International Geoscience and Remote Sensing Symposium (IGARSS-82)* (IEEE, New York, 1982), vol. 2, pp. 6.3–6.5.
9. Egyptian Geological Survey Map 19, scale 1:2,000,000 (1981).
10. We thank Jet Propulsion Laboratory personnel M. Brownell and C. Mahoney and the other members of the SMIRR engineering team for their support in building, calibrating, and integrating SMIRR; H. Paley for her many years of work with the preparation, flight planning, and flight operation of SMIRR; and J. Reimer and E. Abbott for data reduction support. We thank F. El Baz and R. Said for contributions to the interpretation of the data. The research described here was carried out by Jet Propulsion Laboratory under contract with the National Aeronautics and Space Administration and by the U.S. Geological Survey.

20 July 1982

Carbon Monoxide Measurements in the Troposphere

Abstract. *During the second flight of the space shuttle, the measurement of air pollution from satellites (MAPS) experiment in the OSTA-1 payload acquired approximately 35 hours of radiometric measurements of the carbon monoxide mixing ratio in the middle troposphere, upper troposphere, and lower stratosphere. A gas filter radiometer operating in the 4.67-micrometer band was used to acquire the data over the region from 38°N to 38°S during both daytime and nighttime. The performance of the measurement system was excellent. The data reduced to date indicate the presence of significant gradients in the middle tropospheric carbon monoxide mixing ratio with both latitude and longitude over the North Atlantic, the Mediterranean Sea, and the Middle East. On the basis of comparisons with directly measured values, the accuracy of the measurements is approximately 15 percent. Comparisons of data taken on successive orbits over the same geographic region indicate that the repeatability of the measurements is approximately 5 percent.*

This report summarizes preliminary results obtained by the measurement of air pollution from satellites (MAPS) experiment during the second flight of the space shuttle. The major objectives of this experiment are to measure the mixing ratio of carbon monoxide in the middle and upper troposphere as a function of latitude, longitude, and season; to define the operational characteristics of the instrumentation system as part of an orbiting spacecraft; and to evaluate and refine the method of data inference. The MAPS science team (*1*) established that these objectives could be accomplished if a single measurement of ±20 percent accuracy were obtained in at least half of the 10° latitude by 10° longitude grid squares that underlie the orbital track on each of four seasonally spaced flights of the experiment. The flight aboard STS-2 was the first of the series.

The instrument employed is a nadir-viewing gas filter radiometer that operates in the 4.67-μm region of the CO fundamental band with a passband from 2080 to 2220 cm^{-1}. At the surface the instantaneous field of view is approximately 20 by 20 km. The instrument is similar to the selective chopper radiometer (*2*) in that it measures the difference in the upwelling radiation as seen through a vacuum cell and as seen through a cell of fixed pressure and path length containing the gas of interest. Implementation is very different, however, in that the MAPS signal balance between vacuum and gas path legs is continually maintained electronically by an automatic gain control circuit. The instrument evolved as a result of analytical and laboratory studies and aircraft flight tests (*3–7*). The instrument flown on STS-2, which is similar to that described by Ward and Zwick (*8*), is described in detail by Hesketh *et al.* (*9*). It has two 1-cm-long gas cells at different pressures, one containing pure CO at 76 torr and the other pure CO at 266 torr, and a single vacuum cell. This allows the measurement to be made in two broad atmospheric layers, one centered in the middle troposphere (the higher pressure cell) and the other centered in the upper troposphere and lower stratosphere (the lower pressure cell). Since the primary radiation source for the measurement is thermal radiation emitted by the earth's atmosphere, the experiment operates equally well during the daytime or the nighttime and over land or water.

Data from the experiment were formatted and stored on a tape recorder contained within the experiment package. In addition, a 35-mm camera with false-color infrared film acquired overlapping pictures of the daylight portions of the subsatellite track for use in evaluating the effects of the underlying surface and cloud cover.

The scheme for inferring the CO mixing ratio from the calibrated radiometric signals is based on the use of a regression approximation to line-by-line calculations of the atmospheric transmission (*10*). Operationally, line-by-line calculations are made for a set of model atmospheres that is representative of the range of temperature and humidity conditions that existed during the period of the measurements. These calculations yield predicted signal strengths as a function of CO mixing ratio and surface temperature. Regression coefficients, generated from these results for each model atmosphere, yield CO mixing ratios as a direct function of the observed radiometric signals. Actual conditions of atmospheric temperature and humidity along the orbital track are used to select the appropriate blend of coefficients. The actual conditions are obtained from either the U.S. Fleet Numerical Oceanographic Center or the NOAA National Meteorological Center analysis. This method allows the data for cloud-free fields of view to be reduced rapidly and at low cost. Fields of view containing middle-altitude or high clouds require that more highly refined methods be applied.

Correlative measurements were made during the mission. The primary test site was over the eastern United States, where a NASA Learjet carrying an aircraft version of the MAPS radiometer

0036-8075/82/1203-1024$01.00/0 Copyright © 1982 AAAS